International Journal of Heat and Mass Transfer 60 (2013) 252–262

Contents lists available at SciVerse ScienceDirect

International Journal of Heat and Mass Transfer

journal homepage: www.elsevier.com/locate/ijhmt

Effects of surface microstructures of gas diffusion layer on water droplet dynamic behaviors in a micro gas channel of proton exchange membrane fuel cells

Li Chen, Ya-Ling He, Wen-Quan Tao *

Key Laboratory of Thermo-Fluid Science and Engineering of MOE, School of Energy and Power Engineering, Xi'an Jiaotong University, Xi'an, Shaanxi 710049, China

ARTICLE INFO

Article history:
Received 25 June 2012
Received in revised form 16 October 2012
Accepted 5 November 2012
Available online 4 February 2013

Keywords:
Proton exchange membrane fuel cell
Gas channel
Gas diffusion layer
Surface microstructures
Liquid water
Volume of fluid method

ABSTRACT

Numerical simulations using volume of fluid (VOF) method are performed to investigate the effects of the surface microstructures of gas diffusion layer (GDL) on the dynamic behaviors of a water droplet in a micro gas channel (GC) of proton exchange membrane fuel cells (PEMFCs). The detachment size of a droplet under different air velocity and GDL wettability is investigated. Simulation results show that the microstructures of the GDL surface indeed affect the dynamics of water droplets. The directional distributions of carbon fibers in the flow direction are desirable for detaching droplets from the GDL surface and reducing flooding in GC. In addition, a force analytical model is developed, which takes into account the effects of microstructures of GDL surface as well as the surface tension force due to droplet deformation with some simplified assumptions. It is found that surface tension force due to the droplet deformation cannot be simply ignored when analyzing forces acting on the droplet, as the contact angle hysteresis is usually relatively large.

Crown Copyright © 2012 Published by Elsevier Ltd. All rights reserved.

1. Introduction

Many researchers have highlighted the requirement of proper water management in proton exchange membrane fuel cell (PEMFC), and carried out extensive studies to investigate liquid water transport processes in PEMFC. Reviews of these studies have been presented in Refs. [1–3]. To enhance water management, liquid water transport processes in the porous components, namely gas diffusion layer (GDL) and catalyst layer (CL), and in the GC should be fully understood. Liquid water transport process in GDL is essentially the transport process of liquid water in microscopic porous media with anisotropic structures and mixed wettabilities [4,5]. Liquid water transport process in GC is of great importance as GC acts as the first step to distribute reactant to the reactive site and as the last step to drain the liquid water out of PEMFC. This transport process in GC can be generalized as liquid water transport processes in micro channels, which is affected by various operating conditions such as airflow rate [6], inlet humidity [7], operating temperature [8], and operating load [9]. It is also affected by several geometrical parameters including layouts of GC [10], cross sections of GC [11], the number of channels and the land/channel width ratio [12] and GC surface wettability [13].

In the GC, liquid water emerging from the GDL may develop into different flow patterns including films, droplets or slugs, depending on the operating conditions and geometries and wettabilities of GDL and GC [14]. Among them, water droplet movement in the GC is one of the most observed and important phenomena. Using a transparent PEMFC, Yang et al. [14] observed the dynamic behaviors of droplet emergence, growth departure and coalesce. They found that liquid water droplets emerge from GDL at a specific, repeated location at the GDL/GC interface. Theodorakakos [15] experimentally predicted the detachment processes of water droplets in the GC. The dynamic contact angles and detachment size of droplets for the surface of different GDL materials under varying air velocities were investigated in detail. The dynamic behaviors of a droplet are combined results of several forces including shear force, pressure force and surface tension force. Zhang et al. [6] analyzed forces acting on a static water droplet on GDL surface and predicted the detachment diameter of water droplets under different air flow rates. Kumbur et al. [16] proposed a simplified model to predict the onset of water droplet instability on a GDL surface subjected to air flow based on a macroscopic force balance analysis. More recently, Hao and Cheng [17] further took into account the effects of the surface tension force due to the connection between a droplet and the GDL pore which was neglected in Refs. [6,16]. However, they ignored the surface tension force due to droplet deformation in their macroscopic force balance analytical model for the convenience of calculation, leading to underestimation of the droplet detachment size [17].

Obviously, CFD modeling can provide more details of the dynamics of a droplet under various operating conditions and geometrical conditions. Recently, the volume of fluid (VOF) method has also been applied to explore dynamic behaviors of water drop-

* Corresponding author. Tel./fax: +86 029 82669106.
E-mail address: wqtao@mail.xjtu.edu.cn (W.-Q. Tao).

0017-9310/$ - see front matter Crown Copyright © 2012 Published by Elsevier Ltd. All rights reserved.
http://dx.doi.org/10.1016/j.ijheatmasstransfer.2012.11.024

Nomenclature

a	acceleration [m s^{-2}]
A	area [m^2]
b	distance between the top of the droplet and the top face of the control volume [m]
C	volume fraction function
C_1	geometric factor of rough GDL surface
d	carbon fiber diameter [m]; equivalent diameter of the GDL emergence pore [m]
$\mathbf{F}$	momentum source term related to surface tension [N]
g	gravity acceleration [m s^{-2}]
H	height of the GC [m]
l	length [m]
k	mean curvature of the interface [m]
m	mass [kg]
$\mathbf{n}$	surface normal
P	pressure [Pa]
R	radius [m]
t	time [s]
$\mathbf{u}$	velocity vector [m s^{-1}]
U_{in}	average air inlet velocity [m s^{-1}]
w	width of the droplet base [m]

Greek symbols

α	azimuthal angle
ε	porosity
μ	dynamic viscosity [N s m^{-2}]
σ	surface tension coefficient [N m^{-1}]
θ	contact angle [°]
ρ	density [kg m^{-3}]
ν	viscosity [m^2 s^{-1}]
x,y	coordinate

Subscripts

a	advancing contact angle
c	constant
f	fiber
GC	gas channel
in	inlet
k	kth fluid
l	liquid water
g	gas
r	receding contact angle
s	static contact angle
stf	surface tension force

lets in the GC, due to its capacity of considering surface tension force and wall adhesion and of tracking liquid–gas interface [15,18–38]. These studies using VOF can be divided into different categories. For the computational domain, some focused on the GC [15,18–29,36–38], some further considered the cathode of the PEMFC [30–32,35], and some took the whole PEMFC into account [33,34]. For initial liquid water distribution, some started the simulation with initial given liquid water distribution [18–25,30,33,34,37,38] while others performed the simulation with liquid water gradually entering the GC from GDL pores [15,26–29,31,32,35,36]. For the GC bottom surface consisting of GDL, some simply used smooth bottom surface [15,18–29,37,38] while some tried to involve the GDL surface microstructures [24,29,35,36] For the coupling process of liquid water and reactants transport, some concentrated on the liquid water behaviors [15,18–32,36–38] and some further [33–35] simulated the coupled process of liquid water transport and reactant transfer. Note that as a macroscopic interface-capturing method, VOF requires additional artificial algorithms for constructing the phase interfaces; besides, the no-slip boundary condition at the solid surface is inconsistent with the actual moving of the triple-phase line over the solid phase. Since the interface phenomena essentially results from the molecular interactions, some more fundamental methods involving these interactions have been adopted to simulate two-phase flows in GC, such as lattice Boltzmann method (LBM) [17]. Nevertheless, the VOF has shown itself as an powerful and efficient tool for exploring liquid water dynamics in GC, as demonstrated by large amounts of previous studies [15,18–29,36–38].

In PEMFC, the GDL is made of porous materials structured by carbon fibers, such as carbon paper and carbon cloth. In a carbon paper GDL, the carbon fibers are disarranged and misaligned, leading to microscopically complex structures of GDL with random distribution of pore sizes. Therefore, the GDL surface, or the bottom surface of the GC is very rough, as shown in Fig. 1. Obviously, the surface microstructures of the GDL will affect liquid water behaviors in micro GC, since surface tension force, one of the dominant forces acting on a droplet, is closely related to the surface microstructures. As have been demonstrated in the subject studying sliding behaviors of droplets on titled rough surface [39], surface microstructures significantly influence the shape, length and continuity of the triple-phase contact line which is directly related to the water droplet detachment and movement. However, the force analysis method mentioned above usually neglects the effects of GDL surface microstructures, and very few CFD simulations have considered such effects [24,29,36]. Therefore, further work is required to study the effects of the GDL surface microstructures on liquid water behaviors in the GC.

This paper is organized as follows. First, dynamic behaviors of a water droplet in the GC with GDL of different microstructures are studied. Emphasis is placed on the effects of the GDL surface microstructures on liquid water detachment process. Then, an analytical model for predicting the droplet detachment size based on previous studies [16,17] is developed, where the effects of GDL surface microstructures as well as the force due to droplet deformation (both of which are usually neglected in previous studies) are considered. Finally, conclusions are presented.

2. Physical model and numerical method

2.1. Numerical method

CFD commercial software FLUENT 6.3.26 [40] in conjunction with VOF method is used to investigate the liquid water behaviors. FLUENT uses a control-volume-based technique to discretize governing equations into forms that can be solved numerically. Pressure-based segregated solver for an unsteady laminar flow with Green–Gauss cell based gradient evolution and first order implicit temporal discretization are used. An explicit VOF formulation is adopted to track the interface between the liquid water and air. The PISO scheme is used for the velocity–pressure coupling. For all the simulations in this study, the residual of the continuity and velocity are set to 10^{-4} to ensure the simulation converged.

The first algorithm of VOF was developed by Hirt and Nichols [41]. In the VOF method, a volume fraction function C_k of the kth fluid which is computed in each computational cell is defined. $C_k = 1$ means the computational cell is full of the kth fluid, $0 < C_k < 1$ means the computational cell is partially occupied by

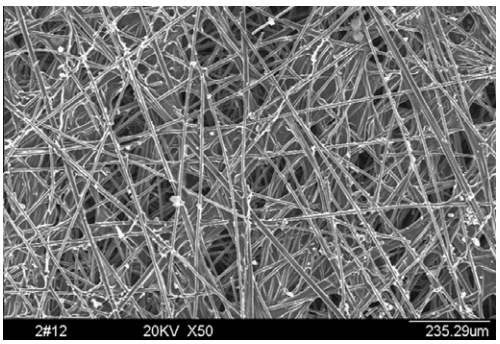

Fig. 1. SEM image of the microstructures of a carbon paper GDL (TGP 60 with 5% PTFE content, taken by the author's group in Xi'an Jiaotong university, China).

the kth fluid, and $C_k = 0$ means there is no kth fluid in the computational cell. The sum of C_k in a computational cell is unit:

$$\sum C_k = 1 \tag{1}$$

The tracking of the interface is accomplished by solving the following equation in each computational cell:

$$\frac{\partial(C_k\rho_k)}{\partial t} + \nabla\cdot(C_k\rho_k\mathbf{u}_k) = 0 \tag{2}$$

where t is the time, ρ is the density and $\mathbf{u}$ is the velocity. The governing equations of velocity field are the continuity equation and the Navier–stokes equation:

$$\frac{\partial(\rho)}{\partial t} + \nabla\cdot(\rho\mathbf{u}) = 0 \tag{3}$$

$$\frac{\partial(\rho\mathbf{u})}{\partial t} + \nabla\cdot(\rho\mathbf{u}\mathbf{u}) = -\nabla p + \nabla\cdot[\mu(\nabla\mathbf{u} + \nabla\mathbf{u}^{\mathrm{T}})] + \rho\mathbf{g} + \mathbf{F} \tag{4}$$

where p is the pressure, ρ and μ are volume averaged density and dynamic viscosity, respectively, which are calculated with linear interpolation using the volume fraction function C_k:

$$\rho = \sum \rho_k C_k \tag{5}$$

$$\mu = \sum \mu_k C_k \tag{6}$$

$\mathbf{F}$ in Eq. (4) is a momentum source term related to surface tension by adopting the continuum surface force (CSF) model [42]:

$$\mathbf{F} = 2\sigma k\frac{\rho\nabla C_k}{(\rho_1+\rho_2)} \tag{7}$$

where σ is the surface tension coefficient and k is the mean curvature of the interface which is computed from the local gradient of surface normal $\mathbf{n}$ at the interface:

$$k = \nabla\cdot\left(\frac{\mathbf{n}}{|\mathbf{n}|}\right) \tag{8}$$

and n is defined as the gradient of C_k:

$$\mathbf{n} = \nabla C_k \tag{9}$$

2.2. Computational domain

In this work, only the microstructures created by fiber ridges are considered, while the microscopic roughness of the individual fiber is neglected. Fig. 2(a)–(c) show three types of microstructures of GDL surface under consideration, where the carbon fibers are represented by lathy rectangles with square cross-section. The carbon fibers are cylinders in practice but here rectangles are used for the purpose of grid generation convenience. In Fig. 2(a), these rectangles evenly crisscross generating uniformly distributed square cavities between adjacent carbon fibers, and this type is called crisscross distribution. The rectangles are only distributed parallel to the flow direction in Fig. 2(b) (called parallel distribution) while they are only aligned orthogonal to the flow direction in Fig. 2(c) (orthogonal distribution). The side length of the square cross section of each carbon fiber is 16 μm, which is somewhat large than the typical diameter of carbon fibers in the GDL of 7 μm. This is because in a real GDL the PTFE coating and overlap of carbon fibers would increase the apparent diameter of carbon fibers. In the study of Park et al. [5], such relatively large fiber size is also used to investigate liquid water transport in a porous GDL. The gap between adjacent carbon fibers is 24 μm. The above structures are somewhat simplified models of the real structures of the GDL. Nevertheless, manufacturing GDL with directional carbon fibers is practically possible as reported by Naing et al. [43].

Fig. 2(d) shows the computational domain composed of a rectangle GC with bottom surface of the GDL with surface microstructures constructed above. The width, height and length of the GC are 340, 300 and 1200 μm, respectively. The size of the GC is typical for micro PEMFC and such size is also widely used in previous studies about liquid water dynamic behaviors in GC [17,26,27]. The bottom surface of the GC, namely the GDL surface, is partly rough with the remaining part being smooth, which is for the consideration of saving computational resources as excessive meshes are required to adequately describe the rough region. However, the part with GDL surface microstructures is sufficiently long, with length of about 680 μm, that the formation, detachment and subsequent movement of a droplet can be completely captured. A square micro-pore with side length of 60 μm is located on the rough GDL surface, which serves as emergence pore where liquid water enters the GC from the GDL. The size of the emergence pore is typical pore size of GDL in practical PEMFC. Similar size is also used in previous studies of liquid water dynamic behaviors in GC. For example, the pore size is 60 μm in Ref. [26] and is 90 μm in Ref. [17]. The whole computational domain is discretized by about 770,000 hex meshes after grid dependence check. The grid independence is checked by using three different grids of 431,650, 770,462 and 908,460 for the crisscross distribution case. Time step is set as 10^{-7} s. The time step independence is checked by using three time steps as 10^{-7}, 1.5×10^{-7} and 88×10^{-8} s for the crisscross distribution case with grids of 770,462. The criteria used for determining the grid and time step dependence is the time evolution of amount of liquid water in the computational domain.

The top wall and two side walls of the GC are hydrophilic with contact angle of 60°. The GDL is hydrophobic with contact angles varying from 120° to 160°. Inlet velocity of the liquid water through the emergence pore is fixed as 0.1 m s^{-1} [26]. For a fuel cell current density as 1 A cm^{-2}, assumed all the water generated is liquid, liquid water generation rate is about 9.34×10^{-5} ml s^{-1} - cm^{-2}. For a reactive area of 10 cm^2, the liquid water injection rate specified here is enough to drain all the liquid water from CL through GDL to the GC. The air velocity at the GC inlet ranges from 5 m s^{-1} to 15 m s^{-1} in the simulations, typical range studied in the literature [17,26]. Outflow boundary condition is applied to the outlet of the GC. No-slip boundary conditions are used for all the solid walls in the computational domain.

3. Results and discussion

3.1. Droplet behaviors in the GC

Figs. 3–5 show the dynamic behaviors of a water droplet in GC with the three different GDL surface microstructures, where the

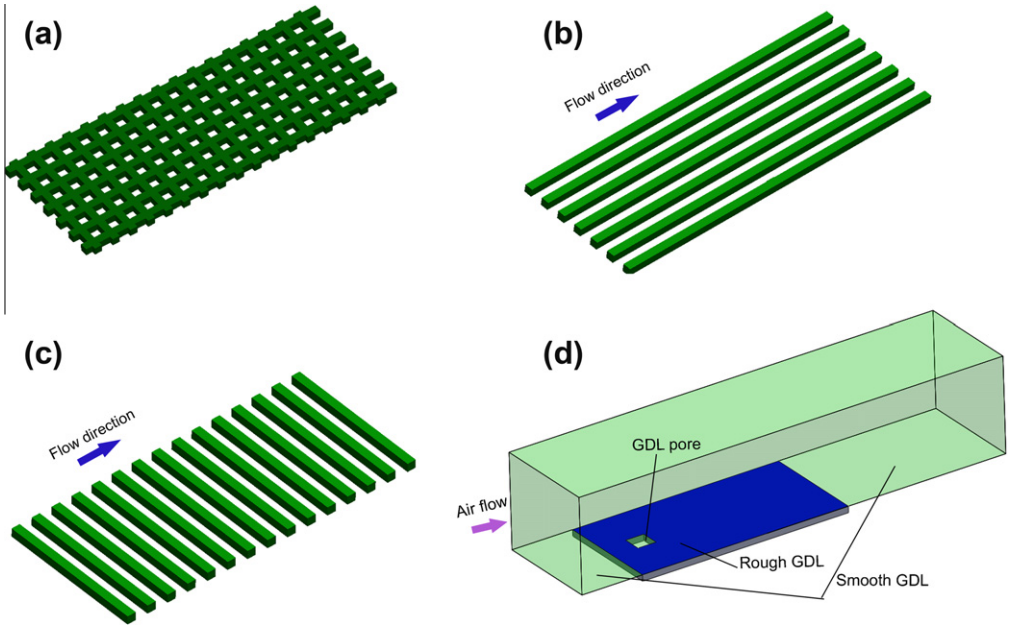

Fig. 2. Computational domain with rough GDL of different surface structures. (a) Crisscross distributions, (b) parallel distributions, (c) orthogonal distributions, (d) the final computational domain composed of a rectangle GC with GDL.

GDL contact angle is 140° and the air inlet velocity is 10 m s^{-1}. It can be observed from the three sets of images that the overall dynamic behaviors of the droplet are similar. Therefore, only the simulation results in Fig. 3 for crisscross distributions of carbon fibers are discussed. In Fig. 3, liquid water enters the GC forming a droplet (Fig. 3(a)). The droplet initially maintains a nearly spherical-cap shape due to the dominated surface tension force (Fig. 3(b)). As the droplet grows bigger, the GC is more blocked and air flow around the droplet becomes increasingly faster. The faster air flow exerts stronger shear force and pressure force on the liquid droplet and thus stretches the liquid water towards downstream (Fig. 3(c)), leading to the formation of a neck between the bulk droplet and the emergence pore. As time progresses, the droplet grows so big that the shear force and pressure force surpass the surface tension force and greatly displace the bulk of the droplet downstream. Consequently, the bulk droplet detaches from the emergence GDL pore and moves rapidly towards the outlet of the GC (Fig. 3(d)). Fig. 3(e) shows the typical flow field around a droplet at $t = 0.00764$ s. The above dynamic behaviors of water droplets in the GC in Figs. 3–5 can be generally described as droplet formation, deformation, detachment and final removal, and are similar to that in Ref. [27], thus validating the simulations of the present study to some degree.

More careful inspection of the simulation results reveals some differences directly caused by the microstructures. The movement of a droplet on the GDL surface is essentially the advancement of the triple-phase contact line, which depends on the shape, length and continuity of the triple-phase contact line. For the parallel distributions, along each fiber the triple-phase contact line is continuous in the flow direction. Thus, for the parallel distributions, the droplet can advance smoothly in the flow direction. For the orthogonal distribution, along each fiber the triple-phase contact line is continuous perpendicular to the flow direction. It appears that the regularly spaced carbon fibers create periodic barriers to the movement of the water droplet in the flow direction, leading to discontinuous movement of the triple-phase contact line in the flow direction. The triple-phase contact line is pinned to the edge of the foremost carbon fiber until the front of the droplet arrives at the next carbon fiber in the flow direction and the triple-phase contact line then jumps to the next carbon fiber. Thus, the triple-phase contact line proceeds in a pin-jump fashion which is different from the continuous movement in the parallel distributions. For the crisscross distributions, the characteristics of movement of triple-phase contact line falls between that for parallel and orthogonal distributions.

Generally, depending on how a droplet forms on a rough solid surface, at least two different wetting types exist. For the first type, the water droplet completely fills the gaps between neighboring rough elements, and such wetting type is described by Wenzel's model [44]. The second type occurs when the water droplet only sits on the top surface of the roughness elements, leaving gas trapped in the gap beneath the droplet, and is described by Cassie's model [45]. In the Cassie's type of wetting, the contact area between the droplet and the rough surface is composite including both water–gas area and water–solid area. Fig. 6 shows the liquid–gas interfaces at certain cross-sections. As can be seen in Fig. 6, all the droplets sit on the top surface of carbon fibers and don't fill the gap between the neighboring carbon fibers, and air pockets are trapped in the gaps. This suggests that Cassie's droplets are formed on the rough GDL surface. Note that if the distance between the adjacent carbon fiber is relatively large, the droplet will infiltrate the gaps and is likely to form a Wenzel droplet. In the above simulation, the distance between neighboring carbon fibers l_f, which can be roughly considered as the pore size of the GDL surface, is 24 μm. Generally, the intrinsic pore size of a carbon paper GDL is in the range of 1–100 μm [46]. In our previous work, we simulated the formation process of a droplet on the hydrophobic GDL surface with crisscross distributions of carbon fibers, where l_f varies from 20 to 60 μm. All the simulation results clearly show the formation of Cassie's droplets on rough hydrophobic GDL surface [36]. In fact, our simulation results agree with the experimental results in Ref. [47] where the transition from Cassie to Wenzel occurs when distance between pillars is greater than 110 μm. It is worth mentioning that the wetting type is not only related to the fiber gap but also related to depth of the gap, and if the depth decreases, wetting type may change to Wenzel's type. In fact, as shown in SEM of the carbon paper GDL (Fig. 1), Wenzel's and Cassie's wetting type coexist when a droplet sits on the GDL surface as

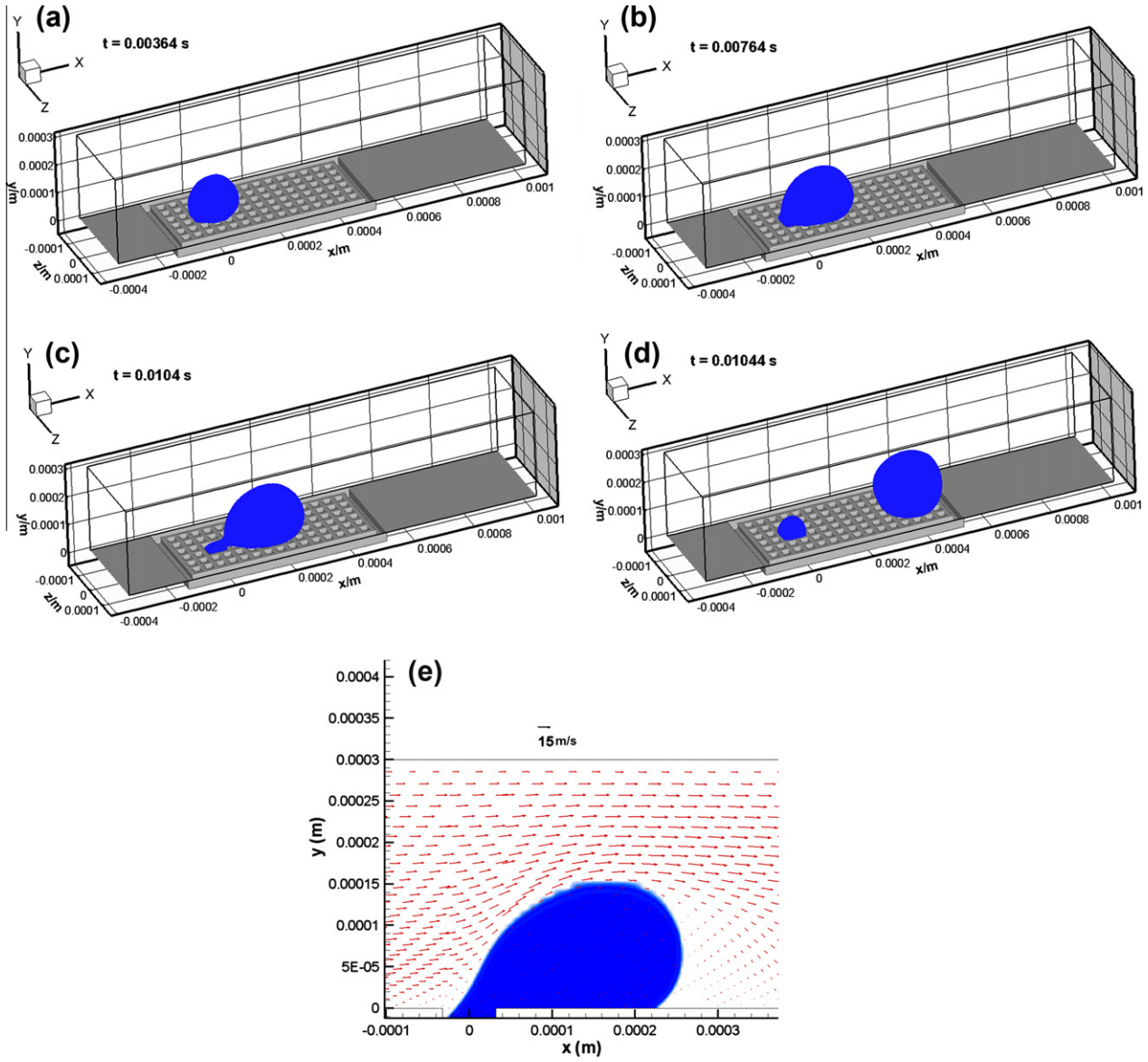

Fig. 3. Dynamic behaviors of the water droplet at the GDL/GC interface for crisscross distribution case with GDL contact angle of 140° and the air inlet velocity of 10 m s^{-1}. (a) t = 0.00364 s, (b) t = 0.00764 s, (c) t = 0.0104 s, (d) t = 0.01044 s, (e) is the flow field around the droplet at t = 0.00764 s.

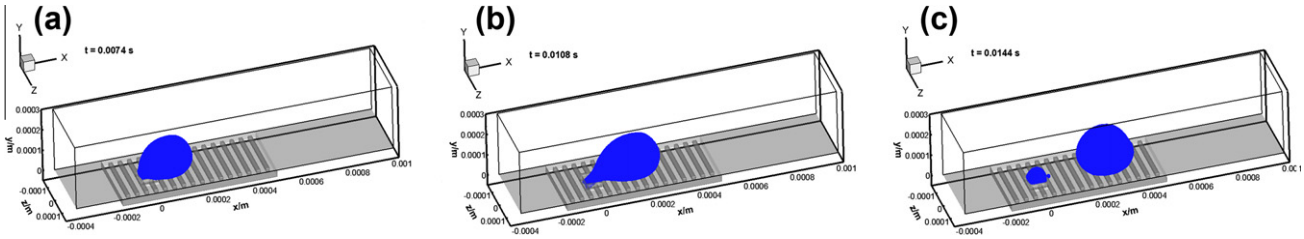

Fig. 4. Dynamic behaviors of the water droplet at the GDL/GC interface for orthogonal distribution case with GDL contact angle of 140° and the air inlet velocity of 10 m s^{-1}. (a) t = 0.0074 s, (b) t = 0.0108 s, (c) t = 0.0144 s.

the depth of pores varies from one layer of fibers to tens of layers of fibers. In the present study, we consider the other layers of the carbon fibers in carbon paper GDL follow the same arrangements of the first layer that described in our simulations (Manufacturing carbon paper GDL with such regular structures is practically possible currently as reported by Naing et al. in Ref. [43]). Thus, each gap between adjacent fibers can penetrate the whole GDL, the depth of which is the thickness of the GDL with typical value of about 200 μm. Under such circumstance, only Cassie's droplets form.

3.2. Droplet detachment size

To further study the effects of the GDL surface microstructures, liquid water transport processes in the GC with GDL with

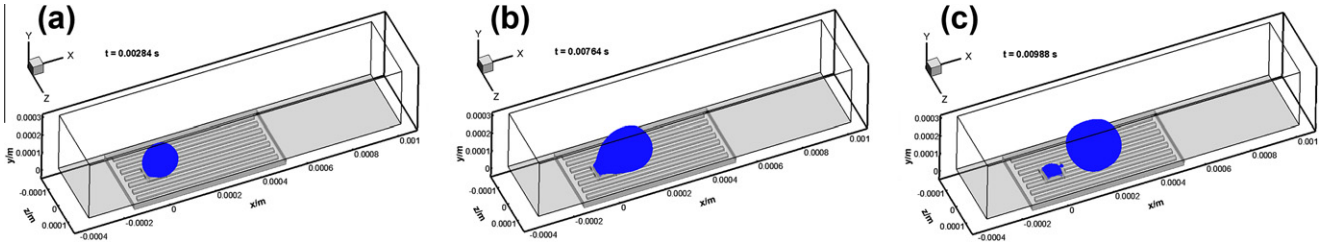

Fig. 5. Dynamic behaviors of the water droplet at the GDL/GC interface for parallel distribution case with GDL contact angle of 140° and the air inlet velocity of 10 m s^{-1}. (a) t = 0.00284 s, (b) t = 0.00764 s, (c) t = 0.00988 s.

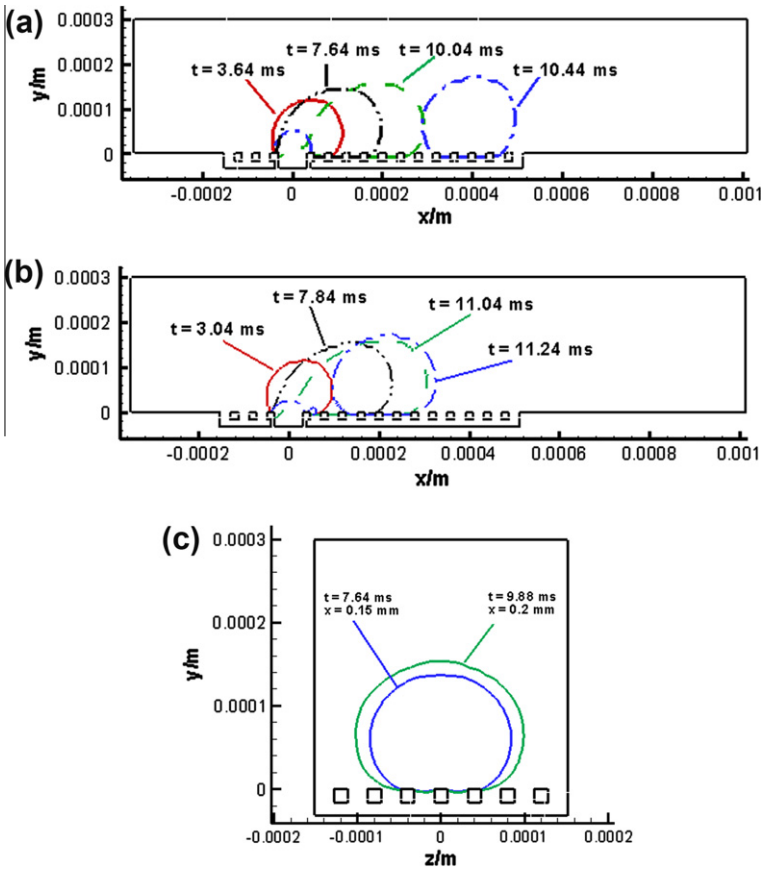

Fig. 6. Liquid–gas interfaces at certain cross-sections of the computational domain. (a) Crisscross distributions, (b) orthogonal distributions, (c) parallel distributions.

surface microstructures, as well as with a completely smooth GDL are simulated under different inlet air velocities U_{in} and GDL contact angles θ. Detachment size (or critical detachment radius), defined as the radius of a sphere the volume of which equals the volume of the droplet just detached from the emerging pore, is an effective measurement of the capacity of a GDL surface to shed droplets. Small detachment size indicates that the GDL surface facilitates the detachment of a droplet adhered to it. Fig. 7(a) and (b) shows the droplet detachment size at different GDL contact angles and different Reynolds number Re, respectively. Re is calculated by $Re = U_{in} d_{GC}/\upsilon_{air}$ with d_{GC} being the hydraulic diameter of the GC. As expected, the droplet detachment size decreases as Re increases or GDL contact angle increases. One interesting observation is that the detachment size for the cases with GDL surface microstructures is always smaller than that for the smooth GDL surface case, indicating that GDL surface microstructures are helpful for shedding the droplet. The effects of the GDL surface microstructures become more apparent for smaller Re or lower GDL contact angle, due to increased contact area between droplet base and the GDL surface. In addition, the detachment size for the three cases with microstructures differs from each other, the parallel distributions result in the shortest detachment size, followed by the crisscross distributions and finally the orthogonal distributions, demonstrating that the parallel distribution of carbon fiber facilitates movement of the droplet in the flow direction in GC. Thus, parallel distributions are the desirable surface structures for reducing the flooding in the GC. As mentioned above manufacturing GDL with directional carbon fibers is practically possible as reported by Naing et al. in Ref. [43].

4. Analytical model for a droplet at the GDL/GC interface

In this section, an analytical model regarding forces acting on a control volume including a droplet is used to predict the drop-

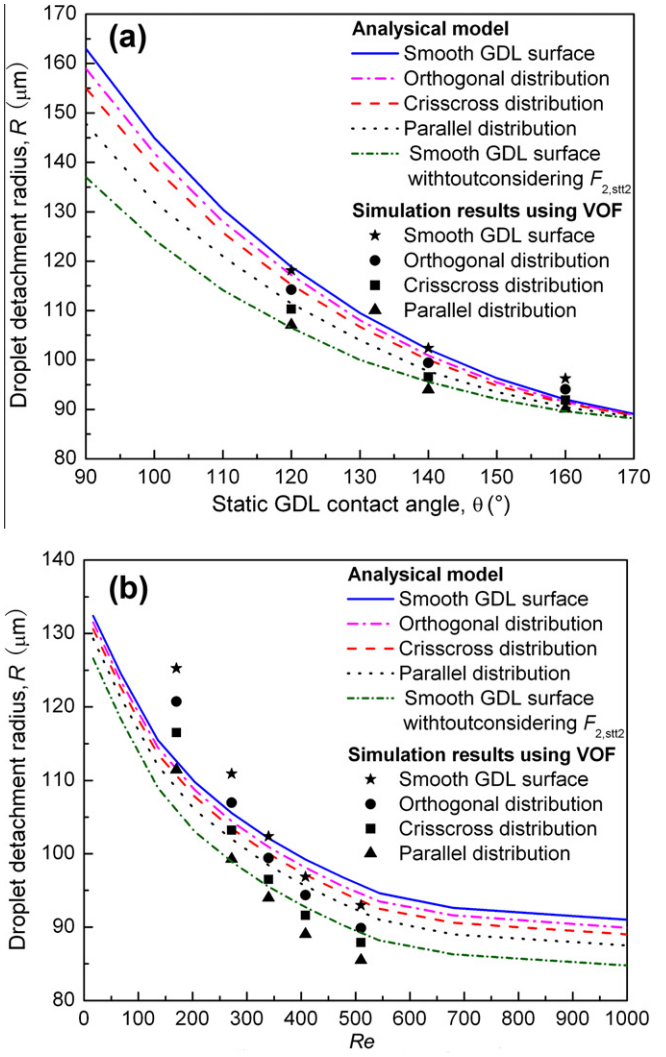

Fig. 7. Numerical results and predicted results using force analytical model for water droplet detachment size. (a) Droplet detachment size at different GDL contact angles, (b) droplet detachment size at different Reynolds number *Re* (defined as $Re = U_{in}d_{GC}/\upsilon_{air}$, where d_{GC} is the hydraulic diameter of the GC, U_{in} is the air inlet velocity and υ_{air} is the dynamic viscosity of the air).

let detachment size at the GDL/GC interface. This model is based on the work of Zhang et al. [6], Kumbur et al. [16] and Hao and Cheng [17]. In the present study, we further take into account the effects of the GDL surface microstructures as well as the surface tension force due to droplet deformation. We propose a scheme to incorporate the effects of the surface microstructures. Fig. 8(a) shows a schematic of a droplet at the GDL/GC interface subjected to air flow. The control volume under consideration is ABDC including the droplet and the air around, with a depth equal to the diameter of the droplet, as shown in Fig. 8(b). Forces acting on the control volume include the pressure force F_p created by pressure difference, shear force F_{shear1} and F_{shear2} generated by the top wall and the bottom wall of the GC, respectively, surface tension force $F_{x,stf2}$ between the bottom wall of the GC and the droplet base and surface tension force $F_{x,stf1}$ between the droplet and the GDL emergence pore. The forces mentioned above are analyzed as follows, with emphasis on the surface tension force due to water droplet deformation and the effects of surface microstructures while the details of other forces can be found in [6,16,17].

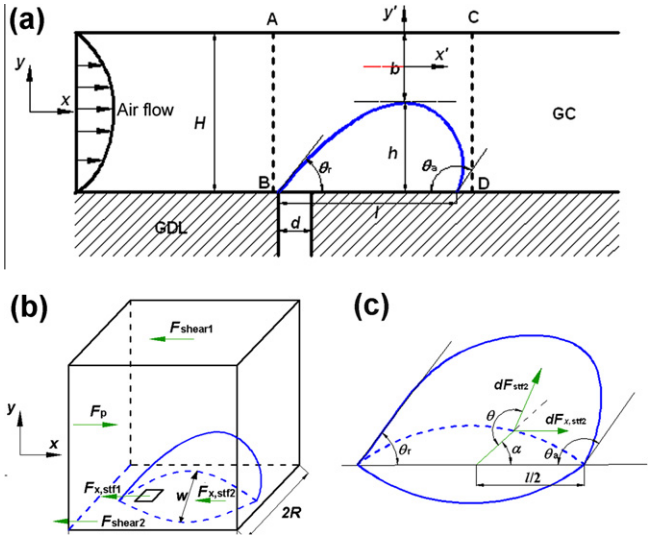

Fig. 8. Schematic of the analytical force balance at the GDL/GC interface. (a) Schematic of a droplet at the GDL/GC interface subjected to air flow, (b) control volume including the droplet and the air around, (c) droplet base.

4.1. Surface tension force due to water droplet deformation

Under the air flow from the inlet of the GC, the triple-phase contact line between the droplet base and the GDL/GC interface is in actual motion. The contact angle around the triple-phase contact line doesn't remain the static contact angle initially given. Instead, it dynamically changes in the flow direction. The dynamic contact angle at the front of the droplet is called advancing contact angle θ_a and that at the rear is called receding contact angle θ_r. Thus, the droplet presents a deformed shape deviating from spherical shape, leading to the surface tension force $F_{x,stf2}$ due to droplet deformation as shown in Fig. 8(c). Fig. 8(c) shows the droplet base, i.e., the contact interface between the bottom of the droplet and the GDL surface. Assume that the droplet base is circular (which is a relatively strong assumption [48], but is widely adopted in previous analysis [16,17]), $F_{x,stf2}$ can be calculated by the following [16]

$$F_{x,stf2} = \int_0^{2\pi} \sigma \frac{w}{2} \cos(\pi - \theta)\cos(\alpha) d\alpha \tag{10}$$

where w is the droplet contact width on the GDL surface orthogonal to the flow direction, which can be obtained by the following expression based on the assumption of circular droplet base

$$w = 2R\sin\theta_s \tag{11}$$

where R is the radius of the droplet, and θ_s is the static contact angle of the GDL surface which equals the contact angle prescribed initially. To calculate the integral in Eq. (10), a relationship between dynamic contact angle θ and the azimuthal angle α is required. Different relationships exist in literature. For example, Ref. [16] suggested that the contact angle lineally changes from the front to the rear of a droplet along the triple-phase contact line, while Ref. [17] assumed that the contact angle at the front half part and the rear half part of a droplet is assumed to be constant advancing or receding contact angle. If the contact angle lineally changes from the front to the rear of a droplet along the triple-phase contact line, $F_{x,stf2}$ becomes [16]

$$F_{x,stf2} = \sigma\pi\frac{w}{2}(\sin\theta_r + \sin\theta_a)\left(\frac{\theta_r - \theta_a}{(\theta_r - \theta_a + \pi)(\theta_r - \theta_a - \pi)}\right) \tag{12}$$

On the other hand, if the contact angle at the front half part and the rear half part of a droplet is assumed to be constant advancing or receding contact angle, respectively, $F_{x,stf2}$ is expressed as [17]

$$F_{x,stf2} = \sigma w(\cos\theta_r - \cos\theta_a) \quad (13)$$

The above analysis of $F_{x,stf2}$ is for the case of smooth GDL surface. To the best of our knowledge, there is no study considering the effects of GDL surface microstructures in literature. In the present study, we try to take into account the effects of GDL surface microstructures. For the GDL with surface microstructures, the droplet formed is Cassie's type and the contact interface is composed of both liquid–solid interface and liquid–air interface. Fig. 9 schematically shows the composite contact interface and the shape of the triple-phase contact line on the GDL with microstructures. Obviously, the composite contact interface generates discontinuous triple-phase contact line, as schematically shown in Fig. 9, which leads to reduced $F_{x,stf2}$. Clearly, the shape and length of the triple-phase contact line greatly depends on the specific structures of the GDL surface, implying that it is difficult to obtain general expressions for $F_{x,stf2}$ on the GDL surface with microstructures as a function of the bulk properties of a GDL. Here, we assume that the ratio of the length of the triple-phase contact line to the whole perimeter of the droplet base equals the porosity of the GDL $(1-\varepsilon)$ with ε as the porosity of the GDL. Thus for the crisscross distribution and parallel distribution, $F_{x,stf2}$ can be calculated by the following expression which is a modified version of Eq. (10)

$$F_{x,stf2} = \int_0^{2\pi} (1-\varepsilon)\sigma\frac{w}{2}\cos(\pi-\theta)\cos(\alpha)d\alpha \quad (14)$$

The porosity ε for crisscross distributions, parallel distributions and orthogonal distributions are calculated by

$$\varepsilon_c = \frac{l_f^2}{(d_f+l_f)^2}, \quad \varepsilon_p = \frac{l_f}{d_f+l_f}, \quad \varepsilon_o = \frac{l_f}{d_f+l_f} \quad (15)$$

respectively, where d_f is the diameter of the carbon fibers and l_f is the distance between the carbon fibers.

Eq. (14) only considers the peripheral triple-phase contact line of the droplet base. Obviously, triple-phase contact line also exists within the contact interface between the droplet base and the GDL surface. However, contact angle difference is not observed in this region, as shown in the dashed circle in Fig. 10. Thus, such inner part of the triple-phase contact line contributes little to the surface tension force $F_{x,stf2}$.

For the orthogonal distribution, the receding contact angle and the advancing contact angle form on the last and the first carbon fiber that contact with the droplet base, respectively, as shown in Fig. 9(c). The two carbon fibers greatly increase the surface tension force as the length of the triple-phase contact line w_1 on them is relatively long. Obviously, w_1 changes as the droplet moves. Here, we simply assume that it can be calculated by the following expression

$$w_1 = C_1 w \quad (16)$$

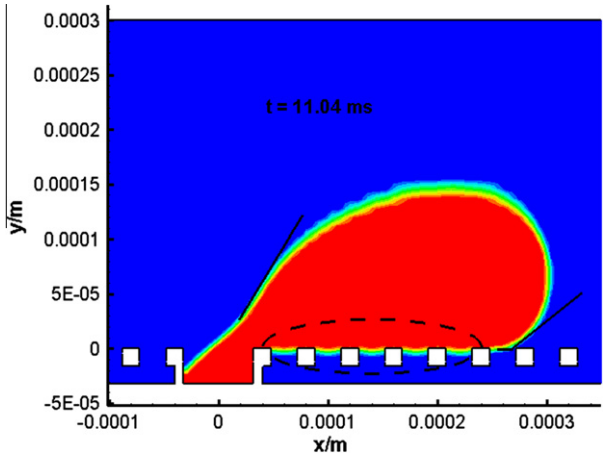

Fig. 10. Contac angles inside the droplet base (for the orthogonal distributions).

where C_1 is a geometric factor. Note that C_1 is not constant because it changes as the droplet moves, and in the present study it is set as 0.1 because this value leads to the best agreement with the numerical simulation results in Section 3. Thus, $F_{x,stf2}$ for the orthogonal distributions of carbon fibers is obtained by

$$F_{x,stf2} = \int_0^{2\pi} (1-\varepsilon)\sigma\frac{w}{2}\cos(\pi-\theta)\cos(\alpha)d\alpha + C_1\sigma w(\cos\theta_r - \cos\theta_a) \quad (17)$$

4.2. Surface tension force due to the connection between the water droplet and the emergence pore

The connection between the droplet and the emergence pore generates the following surface tension force [17]

$$F_{x,stf1} = -\pi\sigma d \quad (18)$$

where d is the equivalent diameter of the emergence pore.

4.3. Shear force on the control volume

When upstream air encounters the droplet, it will flow in the space between the droplet and the front wall (with flow rate Q_1), the back wall (with flow rate Q_2), and the top wall of the GC (with flow rate Q_3). For the convenience of calculating the corresponding shear force, it is commonly assumed that the upstream air flow flows in the space between the droplet and the top wall of the GC [16,17]. Under such assumption, the flow rate between the droplet and the top wall of the GC is $Q = Q_1 + Q_2 + Q_3$, and the total shear force at the front, back and top faces of the control volume now is approximately calculated on the top face of the control vol-

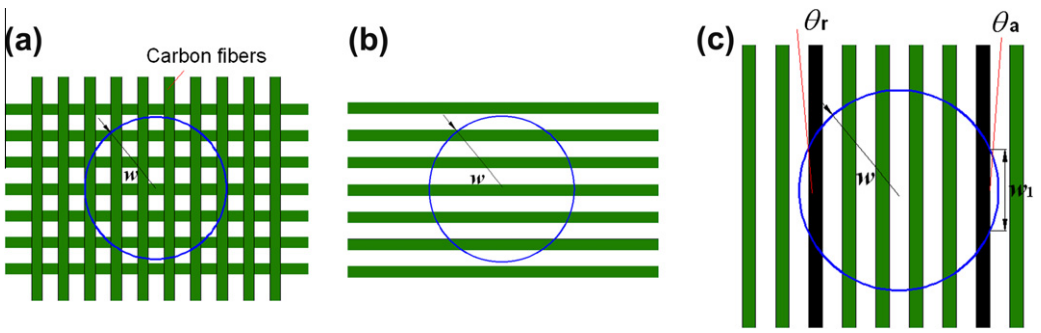

Fig. 9. Droplet base and triple-phase contact line on the GDL surface with microstructures. (a) Crisscross distributions, (b) parallel distributions, (c) orthogonal distributions.

ume (Note that the shear force is a linear function of velocity as shown in Eq. (19), hence it is also a linear function of the volume rate, thus it can be summed up). The air flow exerts a shear force on the top wall of the GC. Thus, the top wall imposes a counter shear force on the top face of the control volume. The shear force can be calculated by [16,17]

$$F_{\text{shear1}} = -\frac{24R^2 H\eta_a U_{\text{in}}}{b^2} \tag{19}$$

where b is the distance between the top of the droplet and the top face of the control volume, H is the height of the GC and U_{in} is the average air inlet velocity (see Fig. 9(a)).

Note that in Ref. [17] an additional assumption is made, namely the droplet should be far from the front wall and the back wall. We consider this assumption is unreasonable. This is because if the droplet is far from the front and back walls, the air flow will mainly flows between the droplet and the front wall (and back wall), rather than flows between the droplet and the top wall. Actually, based on the first assumption that upstream air flow flows in the space between the droplet and the top wall of the GC, we believe that whether the droplet is close to the front and back walls or not has slight effect on the shear force calculated by Eq. (19), as the shear force at the front and back walls have already been implicitly considered in Eq. (19).

Little air flows around the bottom wall of the GC and shear force there can be neglected. Furthermore, the shear force due to the droplet motion also can be ignored because the movement of the droplet is extremely slow. Overall, the shear force on the bottom face of the control volume is negligible.

4.4. Pressure force

The pressure force along the flow direction can be calculated by the pressure difference Δp between the left and right faces of the control volume

$$F_P = \frac{48H^2R^2\eta_a U_{\text{in}}}{b^3} \tag{20}$$

where A is the cross sectional area of the control volume equal to $2wH$.

4.5. Other forces

In the analysis, only forces in the flow direction are considered because liquid water mainly moves streamwisely. Other forces including gravity force, buoyancy force and lift force perpendicular to the flow direction are not taken into consideration. In fact, the above three forces are volume force, which are much smaller compared with other forces, as roughly evaluated in our previous study [36].

4.6. Force balance on the control volume

According to Newton second law, the product of the quality and the acceleration is equal to all the forces acting on the mass

$$F_{\text{sum}} = m_{\text{air}}a_{\text{air}} + m_{\text{droplet}}a_{\text{droplet}} \tag{21}$$

The first term on the right hand is zero due to the fully developed air flow assumed. Further, the second term also can be ignored as the acceleration of the droplet is extremely slow. Thus

$$F_{\text{sum}} = F_P + F_{\text{shear}} + F_{x,\text{stf1}} + F_{x,\text{stf2}} = 0 \tag{22}$$

Substituting the derived expressions of the four forces and replacing b in terms of R, ($b = H - R^*(1-\cos\theta_s)$) lead to the final form of force balance on the control volume

$$\frac{48R^2H^2\eta_a U_{\text{in}}}{(H - R(1-\cos\theta_s))^3} = \frac{24HR^2\eta_a U_{\text{in}}}{(H - R(1-\cos\theta_s))^2} + \pi\sigma d + F_{x,\text{stf2}} \tag{23}$$

In Ref. [17] it is assumed that the droplet keeps a spherical-cap approximately with the neglect of the deviation from the spherical shape. Based on this assumption, surface tension force $F_{x,\text{stf2}}$ was considered to be very small compared with $F_{x,\text{stf1}}$ and was ignored [17]. Such a treatment leads to solution convenience of Eq. (23). However, it does not agree with the practical situation where the droplet greatly deforms before detachment as shown by the simulation results in the present study as well as in the experiments by Theodorakakos et al. [15] (see Fig. 7 in Ref. [15]) and Kumbur et al. [16]. Table 1 lists the receding contact angle and advancing contact angle measured for inlet air velocity of 10 m s^{-1} obtained by the present simulation and the experiments in Refs. [15,16]. It can be seen that the contact angle hysteresis is as much as 70°–90°. Obviously, such considerable deformation of the droplet generates sufficiently big $F_{x,\text{stf2}}$ according to Eq. (12) or Eq. (13). Here, the values of $F_{x,\text{stf1}}$ and $F_{x,\text{stf2}}$ on a smooth GDL surface are roughly estimated. In the estimation, θ_s, θ_a and θ_r are assumed to be constant as 140°, 155° and 70°, respectively, based on the date listed in Table 1. The diameter of the emergence pore d is 60 μm. Fig. 11 shows the variations of the surface tension forces with the width of the droplet base. The droplet base width varies from 100–240 μm, typical value for a droplet on the set of detachment at the GDL/GC interface [16,27]. As shown in Fig. 11, $F_{x,\text{stf2}}$ is comparable to or even greater than $F_{x,\text{stf1}}$ and it cannot be simply neglected.

4.7. Droplet detachment size

Eq. (23) indicates a critical point at which the droplet is on the set of detachment. This point is called the point of instability [16]. Any increase in the driving pressure force at this point will lead to the entrainment of the droplet. Thus, Eq. (23) can be used to predict the critical radius of the droplet prior to its detachment from the emergence pore, which is the key to understand the mechanisms of droplet retention on the GDL surface. Before solving Eq. (23), the main difficulty is to determine the two dynamic contact angles θ_a and θ_r which depend on several parameters including air flow rate in the GC, droplet size and GDL surface wettability and structures [16]. It is difficult to obtain meaningful expressions for the two dynamic contact angles that completely account for all the factors involved. In fact, the mechanism of the formation of the contact angle hysteresis (difference between θ_a and θ_r) is still unclear. In this study, the following expressions are used which are somewhat simple

$$\theta_r = \theta_s - \theta_{w,r}, \quad \theta_a = \theta_s + \theta_{w,a} \tag{24}$$

where $\theta_{w,r}$ and $\theta_{w,a}$ are set to be constant values of 45° and 10°, respectively.

The contact angle at the front half part and the rear half part of a droplet is assumed to be constant advancing or receding contact angle, respectively, corresponding to Eq. (13). Newton iterative method is used to solve Eq. (23) and the critical radius R for different air inlet velocity, GDL static contact angle and GDL emergence pore size are obtained. The predicted results are shown in Figs. 7 and 12. The values of geometrical parameter and physical parameters required for solving Eq. (23) are the same as that in the simulations in Section 3.

Fig. 7(a) shows the dependence of the critical detachment radius on contact angle, together with results obtained from simulations using VOF in Section 3 as well as that predicted using Eq. (24) in Ref. [17] in which $F_{x,\text{sft2}}$ is ignored. It can be observed that ignoring $F_{x,\text{sft2}}$ always underestimates the droplet detachment size, as also reported in Ref. [17]. With this surface tension force taken into account, the present results predicted using Eq. (23) are in better

Table 1
Contact angles of a droplet on the GDL surface with air inlet velocity as 10 m s^{-1}.

GDL	Contact angle			Ref
	Static	Advancing	Receding	
Crisscross distribution	140°	154°	73°	The present study
Parallel distribution	140°	151°	68°	
Orthogonal distribution	140°	149°	64°	
Carbon paper 1	125°	140°	50°	[15]
Carbon paper 2	130°	140°	70°	
PTFE 5%	$\theta_a - \theta_r = 58°$, Obtained by linear interpretation of Fig. 7 in Ref. [16]			[16]
PTFE 20%	$\theta_a - \theta_r = 76°$, Obtained by linear interpretation of Fig. 7 in Ref. [16]			

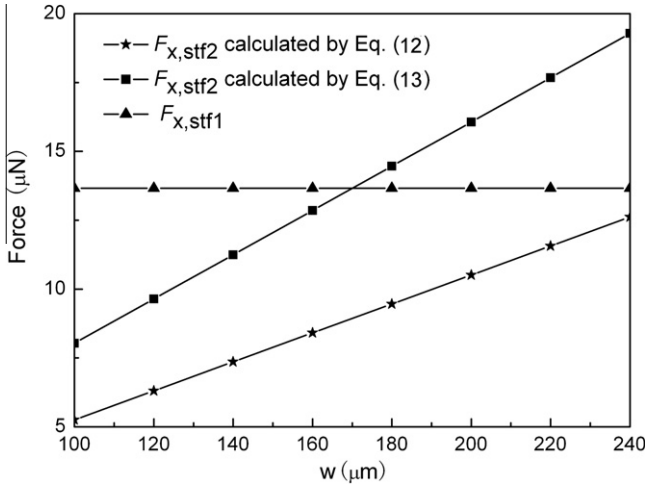

Fig. 11. Evaluation of the surface tension forces acting on a droplet.

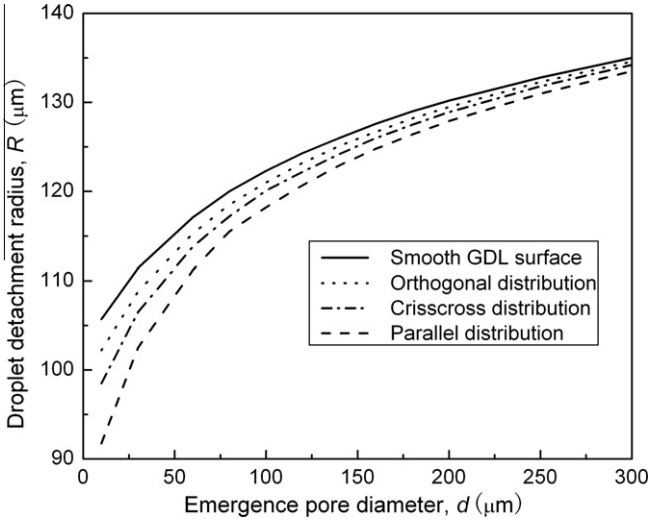

Fig. 12. Droplet detachment radius for different GDL emergence pore size.

agreement with the simulation results. The discrepancies between the present predicted values and the simulation results are mainly due to the simple calculation of the receding and advancing contact angles using Eq. (24). Fig. 7(b) shows the dependence of the critical detachment diameter on *Re*, which confirms the necessity of taking $F_{x,sft2}$ into consideration. The agreement between the predicted value using Eq. (23) in the present study and the simulated results are not perfect for small and high *Re*, compared with that for moderate *Re*. This may be due to the incompletely precise estimation of the hysteresis. The ignorance of the droplet creeping velocity is another possible reason, as pointed out in Ref. [17]. Overall, fully accounting for the contact angle hysteresis is very important to accurately predict the detachment behaviors of the droplet.

Fig. 12 shows the dependence of the critical detachment diameter on GDL emergence pore size. The droplet detachment size increases as the GDL emergence pore size increases, due to increased $F_{x,stf1}$ according to Eq. (18). Besides, effects of the GDL surface microstructures gradually become weaker as the diameter of GDL emergence pore increases, since $F_{x,stf1}$ dominates over $F_{x,stf2}$ for large GDL emergence pore size. Recently, several groups perforated large pores in the GDL, with diameter significantly greater than the average pore size of the GDL [49], to improve the water management within the GDL. Liquid water generated in the catalyst layer permeates the GDL mainly through these large pores, with the remaining space in the GDL freely available for transport of reactant gas. Thus, the modified GDL helps to alleviate the flooding in the GDL and improve the cell performance. However, such design of carving large pores in the GDL may increase the danger of flooding in the GC, as the droplets emerging from these large GDL pores can grow sufficiently big according to the results in Fig. 12. These large droplets can seriously block the GC and cause ineffective distributions of the reactant gas, causing flooding in the GC.

5. Conclusion

In the present study, the formation, growth, detachment and movement of a droplet in the GC are investigated using CFD commercial software FLUENT 6.3.26 in conjunction with the VOF method, with emphasis on the effects of the microstructures of GDL surface. Three surface microstructures of GDL are considered including crisscross distributions of carbon fibers, parallel distributions of carbon fibers in the flow direction and orthogonal distributions of carbon fibers perpendicular to the flow direction. It is found that the surface microstructures do affect droplet detachment and movement in the GC. Liquid water appears to be more likely to form Cassie's droplets at the GDL/GC interface and surface microstructures helps to shed the Cassie's droplet. The specific surface structures of the GDL also affect droplet behaviors and the parallel distributions of carbon fibers show the best capacity of detaching droplet adhered and reducing flooding in the GC. Finally, an analytical force balance model, in which effects of microstructures on surface tension force due to droplet deformation are particularly estimated, is developed to predict the droplet detachment size in the GC. The predicted results confirm the effects of microstructures of GDL surface.

Acknowledgements

The authors thank the National Nature Science Foundation of China (No. 51136004) and National Basic Research Program of China (973 Program) (2013CB228304) for supporting this work.

References

[1] H. Li, Y. Tang, Z. Wang, Z. Shi, S. Wu, D. Song, J. Zhang, K. Fatih, J. Zhang, H. Wang, Z. Liu, R. Abouatallah, A. Mazza, A review of water flooding issues in the proton exchange membrane fuel cell, J. Power Sources 178 (1) (2008) 103–117.

[2] A. Bazylak, Liquid water visualization in PEM fuel cells: a review, Int. J. Hydrogen Energy 34 (9) (2009) 3845–3857.

[3] R. Anderson, L. Zhang, Y. Ding, M. Blanco, X. Bi, D.P. Wilkinson, A critical review of two-phase flow in gas flow channels of proton exchange membrane fuel cells, J. Power Sources 195 (15) (2010) 4531–4553.

[4] L. Chen, H.-B. Luan, Y.-L. He, W.-Q. Tao, Pore-scale flow and mass transport in gas diffusion layer of proton exchange membrane fuel cell with interdigitated flow fields, Int. J. Therm. Sci. 51 (2012) 132–144.

[5] J.W. Park, K. Jiao, X. Li, Numerical investigations on liquid water removal from the porous gas diffusion layer by reactant flow, Appl. Energy 87 (2010) 2180–2186.

[6] F.Y. Zhang, X.G. Yang, C.Y. Wang, Liquid water removal from a polymer electrolyte fuel cell, J. Electrochem. Soc. 153 (2) (2006) A225–A232.

[7] J.P. Owejan, T.A. Trabold, D.L. Jacobson, D.R. Baker, D.S. Hussey, M. Arif, In situ investigation of water transport in an operating PEM fuel cell using neutron radiography: Part 2 – Transient water accumulation in an interdigitated cathode flow field, Int. J. Heat Mass Transfer 49 (25–26) (2006) 4721–4731.

[8] H. Lin, T.-F. Cao, L. Chen, Y.-L. He, W.-Q. Tao, In situ measurement of temperature distribution within a single polymer electrolyte membrane fuel cell, Int. J. Hydrogen Energy 37 (16) (2012) 11871–11886.

[9] N. Pekula, K. Heller, P.A. Chuang, A. Turhan, M.M. Mench, J.S. Brenizer, K. Ünlü, Study of water distribution and transport in a polymer electrolyte fuel cell using neutron imaging, Nucl. Instrum. Methods Phys. Res., Sect. A 542 (1–3) (2005) 134–141.

[10] D. Spernjak, A.K. Prasad, S.G. Advani, In situ comparison of water content and dynamics in parallel, single-serpentine, and interdigitated flow fields of polymer electrolyte membrane fuel cells, J. Power Sources 195 (11) (2011) 3553–3568.

[11] J.P. Owejan, T.A. Trabold, D.L. Jacobson, M. Arif, S.G. Kandlikar, Effects of flow field and diffusion layer properties on water accumulation in a PEM fuel cell, Int. J. Hydrogen Energy 32 (17) (2007) 4489–4502.

[12] A. Turhan, K. Heller, J.S. Brenizer, M.M. Mench, Passive control of liquid water storage and distribution in a PEFC through flow-field design, J. Power Sources 180 (2) (2008) 773–783.

[13] A. Turhan, S. Kim, M. Hatzell, M.M. Mench, Impact of channel wall hydrophobicity on through-plane water distribution and flooding behavior in a polymer electrolyte fuel cell, Electrochim. Acta 55 (8) (2010) 2734–2745.

[14] X.G. Yang, F.Y. Zhang, A.L. Lubawy, C.Y. Wang, Visualization of liquid water transport in a PEFC, Electrochem. Solid-State Lett. 7 (11) (2004) A408–A411.

[15] A. Theodorakakos, T. Ous, M. Gavaises, J.M. Nouri, N. Nikolopoulos, H. Yanagihara, Dynamics of water droplets detached from porous surfaces of relevance to PEM fuel cells, J. Colloid Interface Sci. 300 (2) (2006) 673–687.

[16] E.C. Kumbur, K.V. Sharp, M.M. Mench, Liquid droplet behavior and instability in a polymer electrolyte fuel cell flow channel, J. Power Sources 161 (1) (2006) 333–345.

[17] L. Hao, P. Cheng, Lattice Boltzmann simulations of liquid droplet dynamic behavior on a hydrophobic surface of a gas flow channel, J. Power Sources 190 (2) (2009) 435–446.

[18] P. Quan, B. Zhou, A. Sobiesiak, Z. Liu, Water behavior in serpentine micro-channel for proton exchange membrane fuel cell cathode, J. Power Sources 152 (2005) 131–145.

[19] K. Jiao, B. Zhou, P. Quan, Liquid water transport in straight micro-parallel-channels with manifolds for PEM fuel cell cathode, J. Power Sources 157 (1) (2006) 226–243.

[20] Y.H. Cai, J. Hu, H.P. Ma, B.L. Yi, H.M. Zhang, Effects of hydrophilic/hydrophobic properties on the water behavior in the micro-channels of a proton exchange membrane fuel cell, J. Power Sources 161 (2) (2006) 843–848.

[21] Z. Zhan, J. Xiao, M. Pan, R. Yuan, Characteristics of droplet and film water motion in the flow channels of polymer electrolyte membrane fuel cells, J. Power Sources 160 (1) (2006) 1–9.

[22] K. Jiao, B. Zhou, P. Quan, Liquid water transport in parallel serpentine channels with manifolds on cathode side of a PEM fuel cell stack, J. Power Sources 154 (1) (2006) 124–137.

[23] S. Ebrahim, M. Shila, Deformation of a droplet in a channel flow, J. Fuel Cell Sci. Technol. 5 (4) (2008) 041008.

[24] G. He, Y. Yamazaki, A. Abudula, The effect of wall roughness on the liquid removal in micro-channels related to a proton exchange membrane fuel cell (PEMFC), J. Power Sources 195 (6) (2010) 1561–1568.

[25] N. Akhtar, P.J.A.M. Kerkhof, Dynamic behavior of liquid water transport in a tapered channel of a proton exchange membrane fuel cell cathode, Int. J. Hydrogen Energy 36 (4) (2011) 3076–3086.

[26] X. Zhu, P.C. Sui, N. Djilali, Dynamic behaviour of liquid water emerging from a GDL pore into a PEMFC gas flow channel, J. Power Sources 172 (1) (2007) 287–295.

[27] X. Zhu, P.C. Sui, N. Djilali, Three-dimensional numerical simulations of water droplet dynamics in a PEMFC gas channel, J. Power Sources 181 (1) (2008) 101–115.

[28] X. Zhu, Q. Liao, P.C. Sui, N. Djilali, Numerical investigation of water droplet dynamics in a low-temperature fuel cell microchannel: effect of channel geometry, J. Power Sources 195 (3) (2010) 801–812.

[29] Y. Ding, H.T. Bi, D.P. Wilkinson, Three-dimensional numerical simulation of water droplet emerging from a gas diffusion layer surface in micro-channels, J. Power Sources 195 (21) (2010) 7278–7288.

[30] A.D. Le, B. Zhou, H.-R. Shiu, C.-I. Lee, W.-C. Chang, Numerical simulation and experimental validation of liquid water behaviors in a proton exchange membrane fuel cell cathode with serpentine channels, J. Power Sources 195 (21) (2010) 7302–7315.

[31] K. Jiao, B. Zhou, Innovative gas diffusion layers and their water removal characteristics in PEM fuel cell cathode, J. Power Sources 169 (2) (2007) 296–314.

[32] K. Jiao, B. Zhou, Effects of electrode wettabilities on liquid water behaviours in PEM fuel cell cathode, J. Power Sources 175 (1) (2008) 106–119.

[33] A.D. Le, B. Zhou, A general model of proton exchange membrane fuel cell, J. Power Sources 182 (1) (2008) 197–222.

[34] A.D. Le, B. Zhou, A generalized numerical model for liquid water in a proton exchange membrane fuel cell with interdigitated design, J. Power Sources 193 (2) (2009) 665–683.

[35] L. Chen, T.-F. Cao, Z.-H. Li, Y.-L. He, W.-Q. Tao, Numerical investigation of liquid water distribution in the cathode side of proton exchange membrane fuel cell and its effects on cell performance, Int. J. Hydrogen Energy 37 (11) (2012) 9155–9170.

[36] L. Chen, H.-B. Luan, Y.-L. He, W.-Q. Tao, Effects of roughness of gas diffusion layer surface on liquid water transport in micro gas channels of a proton exchange membrane fuel cell, Numer. Heat Transfer, Part A 62 (4) (2012) 295–318.

[37] S.C. Cho, Y. Wang, K.S. Chen, Droplet dynamics in a polymer electrolyte fuel cell gas flow channel: forces, deformation, and detachment. I: Theoretical and numerical analyses, J. Power Sources 206 (2012) 119–128.

[38] S.C. Cho, Y. Wang, K.S. Chen, Droplet dynamics in a polymer electrolyte fuel cell gas flow channel: forces, deformation and detachment. II: Comparisons of analytical solution with numerical and experimental results, J. Power Sources 210 (2012) 191–197.

[39] Z. Yoshimitsu, A. Nakajima, T. Watanabe, K. Hashimoto, Effects of surface structure on the hydrophobicity and sliding behavior of water droplets, Langmuir 18 (15) (2002) 5818–5822.

[40] I. Fluent, Fluent 6.3 User's Guide, 2006.

[41] C.W. Hirt, B.D. Nichols, Volume of fluid (VOF) method for the dynamics of free boundaries, J. Comput. Phys. 39 (1) (1981) 201–225.

[42] J.U. Brackbill, D.B. Kothe, C. Zemach, A continuum method for modeling surface tension, J. Comput. Phys. 100 (2) (1992) 335–354.

[43] K.S.S. Naing, Y. Tabe, T. Chikahisa, Performance and liquid water distribution in PEFCs with different anisotropic fiber directions of the GDL, J. Power Sources 196 (5) (2011) 2584–2594.

[44] R.N. Wenzel, Resistance of solid surface to wetting by water, Ind. Eng. Chem. 28 (1936) 988–994.

[45] A.B.D. Cassie, S. Baxter, Wettability of porous surfaces, Trans. Faraday soc. 40 (1994) 546–551.

[46] L. Cindrella, A.M. Kannan, J.F. Lin, K. Saminathan, Y. Ho, C.W. Lin, J. Wertz, Gas diffusion layer for proton exchange membrane fuel cells–a review, J. Power Sources 194 (1) (2009) 146–160.

[47] L. Barbieri, E. Wagner, P. Hoffmann, Water wetting transition parameters of perfluorinated substrates with periodically distributed flat-top microscale obstacles, Langmuir 23 (4) (2007) 1723–1734.

[48] Q. Kang, D. Zhang, S. Chen, Displacement of a three-dimensional immiscible droplet in a duct, J. Fluid Mech. 545 (2005) 41–66.

[49] D. Gerteisen, T. Heilmann, C. Ziegler, Enhancing liquid water transport by laser perforation of a GDL in a PEM fuel cell, J. Power Sources 177 (2) (2008) 348–354.